3-D Image-Based Dosimetry in Radionuclide Therapy

M. Ljungberg and K. Sjögreen Gleisner

***Abstract*—Radionuclide therapy is the use of radioactive drugs for internal radiotherapy, mainly for the treatment of metastatic disease. As opposed to systemic cancer therapies in general, the use of radioactively labeled drugs results not only in a targeted therapy but also the possibility of imaging the distribution of the drug during therapy. From such images, the absorbed doses delivered to tumors and organs at risk can be calculated. Calculation of the absorbed dose from 3-D images such as single-photon emission computed tomography (SPECT)/CT, and in some cases positron emission tomography (PET)/CT, relies on image-based activity quantification. Quantification is accomplished by modeling the physics involved in the image-formation process, and applying image-processing methods. From a time-sequence of such quantitative images, the absorbed doses are then calculated. Although individual-patient dosimetry is a standard component of other forms of radiotherapy, it is still overlooked in the majority of radionuclide therapies. In this review, we summarize the physical and technical problems that need to be addressed in image-based dosimetry. The focus is on SPECT, since most of the radionuclides used are single-photon emitters, although the use of PET is also discussed. Practical issues of relevance for the practical implementation of personalized dosimetry in radionuclide therapy are also highlighted.**

***Index Terms*—Absorbed dose, dosimetry, image reconstruction, Monte Carlo, positron emission tomography (PET), quantification, single-photon emission computed tomography (SPECT).**

I. Introduction

RADIONUCLIDE therapy is a radiotherapy modality that is currently increasing in scope and interest. It is based on the internal delivery of unsealed radioactive compounds for the treatment of benign and malignant conditions. The most common applications are the treatment of patients with benign thyroid diseases and thyroid ablation in adults, both of which involve the radioactive substance ^{131}I-NaI [1]. Newer applications include, for instance, the treatment of neuroendocrine tumors using radiolabeled somatostatin analogs, such as ^{177}Lu-Dotatate or ^{90}Y-Dotatoc, intra-arterial treatment of primary tumors or metastases in the liver using ^{90}Y microspheres, and treatment of castration-resistant prostate cancer using $^{223}RaCl_2$ and ^{177}Lu-labeled prostate-specific membrane antigen [1], [2].

The radionuclides employed in therapy have longer physical half-lives than those used for diagnostic applications and emit particles upon radioactive decay, such as electrons in the case of β^- decay or α particles. Many radionuclides emit both charged particles and γ radiation, which enables imaging and subsequent individual-patient dosimetry. The most commonly used radionuclide is still ^{131}I, which has a physical decay half-life of 8.02 days and emits β^- particles as well as γ radiation. Other β^- emitters include ^{177}Lu and ^{90}Y, which have physical half-lives of 6.65 days, and 2.67 days, respectively. Owing to the higher relative biological effectiveness of α radiation, there is currently a notable interest in the development of therapies involving α emitters such as ^{223}Ra, ^{227}Th, ^{213}Bi, and ^{225}Ac.

For radiotherapy modalities in general, such as external-beam radiotherapy and brachytherapy, the quantity used for correlation and prediction of the radiobiological response is the absorbed dose. Absorbed-dose planning is routinely undertaken as a part of clinical treatment, with the aim of maximizing the probability of successful treatment response while keeping the risk of toxicity for organs at risk at justifiable levels. As in conventional radiotherapy, radionuclide therapy induces treatment effects by ionization in tissue and consequential triggering of radiobiological mechanisms, with cell death or fibrosis as possible outcomes. Radionuclide therapy is believed to be particularly useful for disseminated cancer, where conventional radiotherapy is less successful. It is similar to brachytherapy in that the radiation source is located inside the body of the patient, although the means of radiation delivery differs. An advantage of systemically administered radionuclide therapies is that individual clusters of tumor cells need not be defined geometrically before treatment (as part of dose planning). The drawback is then that once the radiopharmaceutical has been administered, the pattern of radiation exposure cannot be manipulated from the outside, i.e., turned on or off, or modulated geometrically. Factors that may modify the radiobiological response are the absorbed dose rate, which is generally lower in radionuclide therapy than in other radiotherapy modalities, and inhomogeneity in the radiation exposure that is intrinsic in therapy delivered on a molecular basis. Nevertheless, there are no reasons to expect the radiobiological mechanisms involved in radionuclide therapy to differ from those of other radiotherapy modalities to the extent that the absorbed dose would not be valuable for providing

Manuscript received May 2, 2018; revised July 4, 2018; accepted July 24, 2018. Date of publication July 26, 2018; date of current version November 1, 2018. This work was supported in part by the Swedish Research Council under Grant 621-2014-6187, and in part by the Berta Kamprad Cancer Foundation under Grant FBKS 2017-37 and Grant FBKS-2017-33. *(Corresponding author: M. Ljungberg.)*

The authors are with the Department of Medical Radiation Physics, Lund University, 22185 Lund, Sweden (e-mail: michael.ljungberg@med.lu.se; katarina.sjogreen_gleisner@med.lu.se).

Color versions of one or more of the figures in this paper are available online at http://ieeexplore.ieee.org.

Digital Object Identifier 10.1109/TRPMS.2018.2860563

a better understanding of the effects (frequency of response and toxicity) seen in patients. Still, radionuclide therapy is handled as a kind of radioactive chemotherapy in most clinical applications, with treatment prescriptions in terms of fixed activities, possibly adjusted based on patient weight or body surface area. The evidence base for the use of personalized dosimetry was reviewed and published in 2014 [3]. Since then, several research studies have focused on the investigation of individual-patient absorbed doses and their relationship with toxicity and treatment response. In particular, the development in ^{90}Y microsphere treatment is notable, and the evidence of dose-effect relationships has been reported for hepatocellular carcinoma [4], neuroendocrine tumor metastases [5], colorectal cancer metastases [6], and for normal liver tissue [4], [7]. The current status in ^{177}Lu and ^{90}Y peptide-receptor radiotherapy was recently reviewed [8], and tumor dose-response relationships have been demonstrated for both ^{177}Lu and ^{90}Y peptide-receptor radiotherapy [9], [10]. Individual-patient dosimetry has the potential for broader application and may provide substantial patient benefits. It is also mandated by the European Directive [11].

II. Internal Dosimetry in Brief

Upon systemic administration of a radiopharmaceutical, it is distributed throughout the body of the patient according to normal physiological mechanisms. The uptake is often governed by the biochemical properties of the pharmaceutical, for which targeting mechanisms may include affinity to receptors or antigens on the surfaces of malignant cells. Following the decay of the radioactive nuclei, both particle and photon radiation may be emitted (depending on the properties of the nucleus), and the kinetic energy carried by the charged particles is generally imparted near the point of decay. The emitted photons can penetrate long distances before interacting, thus enabling imaging of the radionuclide distribution. To estimate the delivered mean absorbed dose, i.e., the mean energy imparted per unit mass of tissue in a given volume, the quantities that need to be determined are: 1) the total numbers of decays occurring in different tissues at different times after administration; 2) the pattern with which the emitted particles and photons impart their kinetic energy; and 3) the mass of the tissue where energy absorption occurs.

The Medical Internal Radiation Dose (MIRD) Committee of the Society of Nuclear Medicine has formalized these quantities in the MIRD schema for radiopharmaceutical dosimetry [12], which is as follows:

$$D = \frac{1}{M(r_T, t)} \sum\nolimits_{r_s} \left[\int_0^{T_D} A(r_s, t) dt \sum\nolimits_j \Delta_j \cdot \phi\left(r_T \leftarrow r_S, E_j, t\right) \right] \tag{1}$$

where D (unit: Gy = J/kg) is the mean absorbed dose in a target region r_T, $A(r_s, t)$ is the activity (unit: Bq) contained in a particular source region r_s at time t, Δ_j is the mean energy emitted per radioactive decay for a particular emission type j, ϕ is the absorbed fraction in r_s, and M is the mass of the target region [12]. The upper integration limit T_D is the time at which the exposure ends and is set to infinity in most cases.

Quantity 1) above is described by the time integral in (1), also called the time-integrated activity coefficient (TIAC), for a given organ or tissue. This parameter is often determined by activity quantification from nuclear-medicine images, i.e., single-photon emission computed tomography (SPECT) or positron emission tomography (PET) images, acquired at a number of points in time after administration of the radiopharmaceutical. Quantity 2) is described by the right-hand summation (performed over all emission types). This parameter is calculated using Monte Carlo techniques, implemented either for reference geometries [13], [14] or directly on the nuclear-medicine images. Quantity 3) is described by the division by the mass of the target region. Intrinsic in the MIRD schema are the definitions of the target and source volumes, which for therapy applications need to be defined for individual patients, for instance based on segmentation of anatomical images (CT or MR) or functional nuclear-medicine images (SPECT or PET). In many cases, the major source of uncertainty is probably the estimation of the activity that underlies the estimation of the TIAC.

Alpha-particle therapy can provide locally high-energy deposits due to its high linear energy transfer (LET) and short track-length. The delivered absorbed doses will thus be sensitive to the microscopic distribution, as summarized by Sgouros *et al.* [15]. Because of the short α-particle range, the energy delivery is nonhomogenous, which makes it difficult to estimate the proper volume or mass, and the energy is deposited as per (1). Present clinical imaging systems do not allow for resolution at such a small-scale nonhomogeneity; therefore, the use of model-based methods may be required for absorbed-dose estimation in patients.

III. Quantitative Imaging

The basis for 3-D imaging by scintillation or PET cameras is the acquisition of 2-D data from different angles around the patient. Photons are emitted from the patient in different directions, and some reach the camera and interact with the detector crystals. When the energy absorbed by the crystal(s) is within the preset energy window(s) or is detected in coincidence with lines of response (LORs), it is registered as a count. The acquired projection data do not contain information about the distances between the detectors and points of origin of the photons that produced the counts. This information is achieved by means of tomographic reconstruction, which is performed with the objective of determining the 3-D count distribution (or count rate) that correctly represents the activity distribution generating the set of acquired 2-D data. In most cases, the activity is assumed to be stationary during the acquisition period, meaning that the projection data acquired at different angles only depend on the photon-radiation transport from the point of decay to the camera detectors.

Since most dosimetry studies are performed by SPECT imaging, the sections below will cover quantitative SPECT in detail, while PET will be addressed more briefly. The role

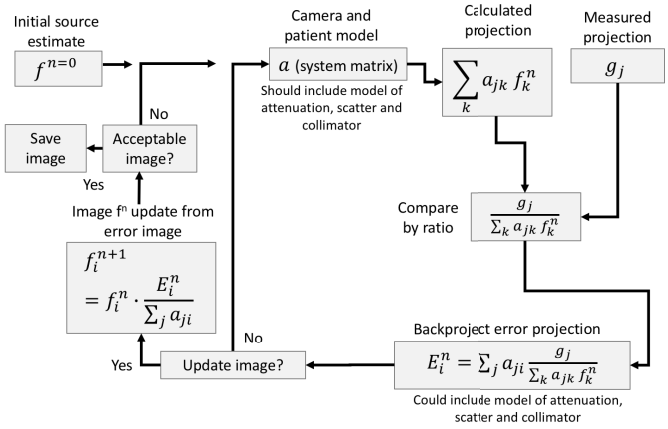

Fig. 1. ML-EM/OS-EM reconstruction principles.

of PET within the context of dosimetry will be discussed in Section V.

A. Tomographic Image Reconstruction

Today, tomographic reconstruction in SPECT and PET is mainly implemented by iterative methods, in which estimated projections, obtained from a computer model of the imaging system and patient, are compared to those actually measured. The most commonly used comparison method is maximum likelihood expectation maximization (ML-EM), as described by

$$f_i^{n+1} = \frac{f_i^n}{\sum_j a_{ji}} \sum_j a_{ji} \frac{g_j}{\sum_k a_{jk} f_k^n} \tag{2}$$

where f_i^n and f_i^{n+1} are the estimated source value in voxel i in the image for iterations n and $n+1$, respectively; g_j is the measured number of counts in projection bin j; and a_{ji} is the system matrix, describing the probability that photons detected in projection bin j originate from voxel i. The elements of the system matrix depend on the patient and camera geometry and the photon energy. A flow chart of (2) is provided in Fig. 1. Starting from an initial estimate of the 3-D source distribution (which is often uniform), the system matrix is applied for propagation into calculated projection data. These are compared to the measured projection data, and an error image is formed from the ratio of the two projection data sets. The initial estimate is then updated using the so-called error image. This process is repeated in an iterative manner, in which the estimated 3-D distribution is updated in each loop.

When the current estimate is no longer updated, within some tolerance level, it is assumed that convergence has been reached and that the estimated 3-D source distribution represents the unknown activity distribution in the patient. However, noise is also present in the detected projection data, which propagates to the estimated count distribution. The amplitude of this noise increases through the iterations, and when many iterations are performed, the signal-to-noise ratio (SNR) of the reconstructed image may decrease. The number of iterations to use in the reconstruction is not determined automatically, but rather needs to be selected by the user, where the choice largely depends on the clinical question at hand. For diagnostic investigations, where the administered activity is comparably low and a low SNR is usually unacceptable, a lower number of iterations is often used. For quantitative imaging, where it is important that the mean count level in an object represents the activity as well as possible, a higher number of iterations is generally required. An additional issue to consider when setting the number of iterations is that the convergence rate is object-dependent. The mean count levels of larger structures converge after fewer iterations than those of smaller structures, and for small structures located near larger structures, the convergence is even slower. For quantitative tumor imaging, e.g., where it is necessary both to segment dosimetric volumes and to determine the mean count level accurately, it may be necessary to use two reconstructed images, one with a low number of iterations and one with a high number [16].

In ML-EM, the error image is calculated from all of the acquired projections before proceeding to the update step. A version of this method in which the convergence rate is accelerated is ordered subset expectation maximization (OS-EM) [17]. The difference between OS-EM and ML-EM is mainly related to the stage of the reconstruction process in which the updates are performed. In OS-EM, the error image is produced from a subset of the projection angles and the update is then made, while in ML-EM the error image is calculated from all of the projection data. Thus, for a single iteration (i.e., when all of the projection data have been processed), the OS-EM method has updated the estimated image a number of times that equals the number of subsets. Thus, the estimated image will converge after fewer iterations of OS-EM, as compared to ML-EM.

The correctness of the estimated images is directly related to the representativeness of the computer models of the camera and radiation transport and the description of the patient geometry, which together form the system matrix. Thus, if some physical effect, such as attenuation, is excluded from the computer model of the patient, the reconstruction will still converge, but the estimated image will not be correct, since the measured and calculated projections will not have been created under the same circumstances.

B. Physical Effects to Model

The three most important physical features that affect the activity quantification are: 1) the photon attenuation in the patient; 2) the counts that arise due to photons that are scattered in the patient and camera; and 3) the limited spatial resolution and penetration effects related to the collimator design. These physical effects can be compensated for by including them in the system matrix, i.e., the model used in the forward and backward projectors in the tomographic reconstruction.

Attenuation: Photon attenuation can be modeled using a 3-D map of the attenuation coefficients $\mu_{i,j,k}$ of the tissues in the patient, where (i, j, k) designates Cartesian coordinates. The values of these coefficients are mainly governed by the atomic number and mass density of the tissue and are used to calculate the probability that a photon will travel farther than a distance

x in an environment described by the distribution of μ values. If x is the distance from the point of photon emission to the surface of the patient in a given direction, the probability that the photon will exit the patient is

$$P(\mu, x) = e^{-\sum_n \mu_{i,j,k}\Delta x} = e^{-\bar{\mu}x}. \quad (3)$$

$\mu_{i,j,k}$ can be estimated from a CT study of the patient and applying previously measured calibration data. The conversion from the Hounsfield units (HU) of the CT image to attenuation coefficients can be performed in different ways, either by using direct relationships between the attenuation coefficients for the relevant photon energy and HU [18], [19] or an indirect relationship between the mass density and HU, from which each attenuation coefficient is determined by multiplying the obtained mass density with the tabulated mass-attenuation coefficient for the relevant energy [20]. For multienergy window acquisitions, attenuation correction can be made separately for the data from each energy-window. It can also be made based on the sum of the acquired data using an effective attenuation coefficient, obtained as the weighted average attenuation by the intensity of each photon emission [19]. In both the cases, the down-scatter from higher photon energies into lower energy windows needs to be considered.

In the forward projector of an ML-EM/OS-EM algorithm, a projection value can be calculated from the current estimate by summing the voxel values along a line extending from the point of photon emission to the detector bin. In SPECT imaging, the effects of attenuation can be modeled by calculating the probability of the escape of photons (3) that are emitted from a particular voxel location and multiplying this probability times that voxel value. This process is conducted for each voxel value along the projection line, and after summation, an attenuated projection value is obtained. In PET imaging, the probability of coincident photon detection is the product of the conditional probabilities that both annihilation photons escape the object

$$P(\mu, x) = e^{-\bar{\mu}_1 x_1} \cdot e^{-\bar{\mu}_2 x_2} = e^{-\bar{\mu}T} \quad (4)$$

where $T = x_1 + x_2$ is the total path length through the patient that the two annihilation photons traverse before reaching the detectors and $\bar{\mu}$ is the average attenuation coefficient along T. Thus, the correction for attenuation becomes independent of the position at which the annihilation occurred along the LOR. To estimate both $\overline{\mu}$ and T, reprojection through the CT image can be performed. A potential advantage of PET imaging is that the attenuation correction can be directly applied to the acquired sinograms.

Because attenuation makes projection values smaller, the voxel source strength will increase during iteration. Thus, accurate modeling of the attenuation properties of tissues translates into accurate attenuation correction.

Scatter: NaI(Tl)-based scintillation cameras have relatively poor energy resolutions, with full-widths at half-maximum (FWHMs) at 140 keV typically between 8% and 10% for modern cameras, and even higher for older cameras. For SPECT imaging, it is desired to register as many full-energy absorptions of the particular photon energy as possible, and relatively large energy windows are thus often used. However, the limited ability to discriminate between photon energies unavoidably results in the detection of photons scattered at small angles. The resulting counts are misplaced in the sense that the origin of each one is not the original point of photon emission, but the point at which the photon was scattered. This unwanted contribution results in a loss of image contrast and, if not compensated for, an overestimated activity with a magnitude that depends on the photon energy and the size and composition of the object.

TABLE I
P/T RATIOS FOR THREE RADIONUCLIDES AND TWO COLLIMATORS

Radionuclide	Collimator	Energy window (keV)	P/T ratio (%)
^{177}Lu	ME	113 ± 10%	30
		208 ± 7.5%	66
	HE	113 ± 10%	31
		208 ± 7.5%	67
^{90}Y	ME	150 ± 30%	6.6
	HE		12
^{131}I	ME	364 ± 7.5%	20
	HE		40

To exemplify how scatter and septal penetration contaminate the data acquired by a scintillation camera, Monte Carlo simulations were performed. A generic scintillation camera [3/8" NaI(Tl) crystal and 9.5% FWHM energy resolution] was modeled, and point sources of ^{177}Lu, ^{90}Y, and ^{131}I were placed in the center of a cylindrical water phantom of radius 11 cm and length 20 cm. Fig. 2 shows the energy pulse-height distributions for the three radionuclides, each calculated for both a medium energy (ME) collimator and a high energy (HE) collimator. The contributions to the totally detected spectra from the primary events, i.e., un-scattered and geometrically collimated events, are plotted separately.

For ^{177}Lu, the primary events constitute the majority of the events in the 208 keV energy window for either collimator, while for the 113 keV energy window there are relatively few primary events and the unwanted events (scatter and penetration events) dominate. For ^{90}Y bremsstrahlung imaging, the primary events constitute a small part of the detected spectrum and the numbers of scatter and penetration events increase rapidly with decreasing energy. Since no distinct photopeaks exist, the choice of an energy window is difficult. For ^{131}I, the photons with high energies of 637 keV (7.12%) and 723 keV (1.79%) contribute significantly with events in the 364 keV energy window, even when using the HE collimator. The ratio of the number of primary events to the total number of events (the P/T ratio) was also calculated in energy windows that are often applied for these radionuclides (Table I). For ^{90}Y and ^{131}I, the P/T ratio is higher for the HE collimator than for the ME collimator, while for ^{177}Lu both collimators yield approximately the same P/T ratio.

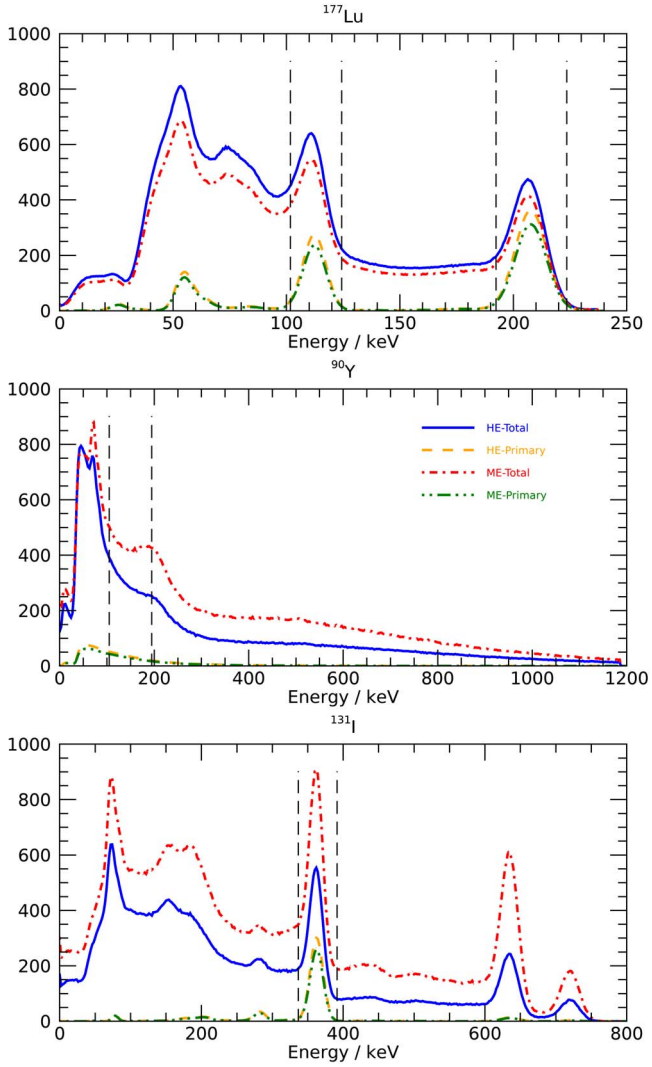

Fig. 2. Energy pulse-height distributions for ^{177}Lu, ^{90}Y, and ^{131}I and HE and ME collimators. Each spectrum is separated into two components: all of the detected events and the primary (un-scattered and geometrically collimated) events. The vertical lines indicate the typically applied energy windows.

Two different types of methods, namely, energy-window-based methods and model-based methods, are used to correct for scatter in iterative methods. Methods of the first type are probably the most commonly used and are based on the assumption that projections acquired in additional energy windows can be used to estimate the contribution from scatter in the main photo-peak window. Common methods include the dual- and triple-energy-window methods [21]. In ML-EM/OS-EM reconstruction, the preferred means of using scatter-window data is adding the scatter estimate in the forward-projector step. This technique yields fewer problems associated with noise than subtracting the scatter estimate from the measured projections. Model-based scatter correction methods have been investigated for many years, ranging from a description of scatter as a mono-exponential function [22] to more spatially variant Monte-Carlo-based scatter functions [23], [24]. One such method that has proven useful is the effective scatter source estimation (ESSE) method [24], in which Monte-Carlo-based precalculated kernels are used to model the scatter within the reconstruction. The main drawbacks of model-based methods are the complexity associated with the generation of scatter kernels and the fact that these kernels are often calculated from a simplified model of the object.

In PET imaging, if scattering of one or both annihilation photons occurs in the patient, a false LOR will be generated. One means of reducing scatter is using an energy window that covers the 511 keV photopeak only. However, the probability that the first interaction in, for example, a lutetium–yttrium oxyorthosilicate (LYSO) crystal is caused by Compton scattering is about twice the probability of photo-electric absorption. For small detector elements, the probability of escape of the Compton-scattered photon is relatively high, which will then produce a loss of true coincidences. Moreover, the energy resolutions of modern crystal materials are relatively poor [on the order of 10%–13% FHWM for 511 keV as compared to about 6%–7% for NaI(Tl) for the same energy], so photons scattered at small angles are not completely rejected by energy discriminators. Scatter correction can be implemented based on scatter function modeling and applying convolution/deconvolution techniques, and more recently by using the single-scattering simulation algorithm. Here, the scatter contribution to a particular LOR is estimated as a grid of probabilities obtained from first-order Compton-scattered photons using the Klein–Nishina cross section. A review of the scatter correction methods used in PET is available in [25], among other literature.

Collimator Effects: The spatial resolution of a scintillation camera system depends mainly on the collimator and intrinsic resolution. If a radioactive source is placed in air and within a reasonable distance from a camera equipped with a parallel-hole collimator, the response, in terms of the number of counts in the field of view of the camera, remains constant regardless of the source-to-camera distance. This characteristic can be understood as follows. For a parallel-hole collimator, the probability that a photon will pass through a hole is restricted by the acceptance angle $\theta = \text{atan}(d/l)$, where d is the hole diameter and l is the collimator thickness. For a single hole that is centered exactly opposite the source, the number of photons that pass through the hole decreases as a function of the square of the source-to-collimator distance. Simultaneously, the number of additional collimator holes that the photons can pass through increases with the square of the source-to-collimator distance. Thus, these two dependencies cancel each other until the source-to-collimator distance is so large that photons, still with angles within the acceptance angle, pass beside the collimator.

While the count rate obtained in response to a point source is independent of the distance, the count distribution depends strongly on the source-to-camera distance. To some degree, it is possible to compensate for this blurring effect in iterative reconstruction by modeling the collimator response function for different source-to-collimator distances in the forward and backward projector steps. For a given collimator, the geometrical resolution (assuming no penetration through the walls) can be modeled as a Gaussian function with a distance-dependent

TABLE II
ABSOLUTE DETECTION EFFICIENCY IN THE PHOTOPEAK WINDOW AS A FUNCTION OF ENERGY FOR THREE DIFFERENT CRYSTAL THICKNESSES. THE LOWER ROWS SHOW THE VALUES RELATIVE TO THOSE OF THE 3/8" CRYSTAL

Crystal thickness	113 keV	140 keV	172 keV	208 keV	245 keV	364 keV
3/8"	0.98	0.91	0.77	0.63	0.52	0.35
5/8"	1.00	0.98	0.91	0.80	0.70	0.51
8/8"	1.00	1.00	0.98	0.93	0.86	0.68
5/8" to 3/8"	102%	108%	118%	128%	135%	145%
8/8" to 3/8"	102%	110%	127%	148%	165%	195%

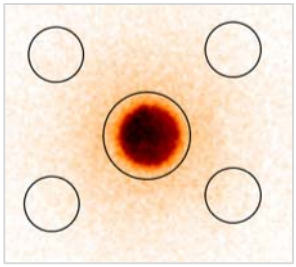

Fig. 3. Determination of the planar system sensitivity in air, used for conversion from detected count rate to activity in quantitative SPECT. The central ROI encompasses the flat activity source, while the four outer ROIs are used for background subtraction.

FWHM. When septal penetration occurs, such as in ^{131}I SPECT imaging, models more sophisticated than Gaussian functions may need to be invoked, for instance by employing Monte Carlo methods.

In PET imaging, the spatial resolution depends on several factors. The detector width is important and has been limited by the size of the photomultiplier tubes (PMTs), although the apparent size has been reduced to less than the physical size by using block-based crystals combined with position-sensitive PMTs and Anger logic for energy-weighted positioning. Another factor is the range of the positrons, since a PET image essentially reflects the positions at which the annihilations occur rather than those of the radionuclide decays. The occurrence of false LORs also degrades the spatial resolution. False LORs can be caused by annihilations that occur before the photons have lost all of their kinetic energy, and consequently the two annihilation photons will not be emitted in exactly opposite directions. False LORs can also be caused by impinging photons penetrating the crystals they entered and instead interacting in neighboring crystals. This depth-of-interaction effect is mainly related to the relatively high photon energy and increases for annihilation sites away from the axial center because of the increasingly oblique angles at which the photons enter the crystals. For further information about how these effects can be modeled in a system matrix, see, for example, the review by Rahmim *et al.* [26].

C. Conversion From Counts to Activity

The system sensitivity of a scintillation camera is mainly governed by the crystal thickness and the collimator used. Most scintillation cameras are optimized for diagnostic applications with ^{99m}Tc with a principal photon energy of 140 keV, for which a thin crystal (3/8") provides a reasonable compromise between detection efficiency and intrinsic spatial resolution. Radionuclides used for radionuclide therapy, such as ^{177}Lu, ^{131}I, ^{90}Y, and ^{111}In, emit photons of higher energies. Table II shows the absolute detection efficiency for three crystal thicknesses and the efficiency relative to a 3/8" crystal. An increased crystal thickness can either improve the counting statistics for a particular acquisition time or reduce the acquisition time for a given noise level.

For quantitative SPECT imaging, there is currently no standardized method of determining the calibration factor, i.e., the factor for conversion from count rate to activity in each voxel of the reconstructed image (unit: MBq^{-1}s^{-1}). There is increasing scientific interest in this area, and different approaches have been proposed [27]–[31]. In an extensive uncertainty analysis of ^{177}Lu SPECT image quantification for renal dosimetry [32], it was found that the calibration factor was the most important contribution to the overall uncertainty in the dosimetric procedure, besides partial volume correction.

Quantitative SPECT images are usually calibrated so that the voxel values represent the activity in a volume corresponding to the voxel volume. In PET imaging, it is customary to perform calibration in terms of activity concentration.

When the tomographic reconstruction is implemented accurately, including accurate modeling of the effects of attenuation and scatter in the projections, appropriate normalization to the frame time and number of acquisition angles, and correct normalization of any filters used, the reconstructed SPECT image represents the count distribution as if the counts were caused by activity in air. The majority of the contributions from scatter and septal penetration, shown in Fig. 2, as well as the effects of attenuation, are thus accounted for in the tomographic reconstruction, and the resulting counts are mainly those caused by primary events. For an SPECT image acquired using parallel-hole collimators, calibration can then be performed by acquiring a planar image, i.e., one projection, of a thin layer of activity in a thin source, for instance in a Petri dish, placed in air. The count rate in air is thus determined from the total count in a region of interest (ROI) surrounding the source in the image, with the background count determined from ROIs placed outside the source subtracted (Fig. 3).

By division by the acquisition time and the contained activity, the calibration factor is obtained. When necessary, the contributions from scatter and septal penetration may be accounted for in the calibration geometry. For ^{131}I, where septal penetration is a prominent component, our group utilized measurements of several flat sources with increasing diameters [33]. The calibration factor for a source with zero diameter was then determined by extrapolation from a fitted line to the sensitivity for each source diameter. This calibration factor was assumed to represent a situation in which the contributions from scatter and septal penetration were negligible and was in good agreement with the value obtained from Monte Carlo simulation of the geometric component in the same geometry [33]. Zhao *et al.* [29] compared the performance

of different calibration methods and concluded that a planar acquisition of a point source was sufficiently accurate when scatter and background correction was included in the determination of the calibration factor. Anizan *et al.* [27], [28] investigated the use of sealed ^{133}Ba sources as ^{131}I surrogates, with detailed analysis of the factors affecting the repeatability and stability. A general uncertainty analysis of the calibration procedure was also undertaken [34].

In clinical systems, tomographic reconstruction methods are not always properly normalized, and it may be necessary to determine the calibration factor from reconstructed images, using the same acquisition and reconstruction protocols that are employed in patient studies. Different calibration geometries have been proposed. One option is to use a homogeneously mixed source with a known activity concentration and a diameter that is sufficiently large so that effects of resolution-induced spill-out become negligible when the source boundaries are excluded from the analysis [35], [36]. Such geometry is generally used for absolute calibration of PET systems [37].

We would like to draw attention to the advantage that the raw data, i.e., the projection data, are easily accessible in gamma-camera imaging, unlike in other tomographic methods, such as PET. As the number of reconstructed counts in an object is sensitive to the number of iterations, the use of filtering or collimator-response compensation, as well as the underlying activity distribution that affects the rate of convergence, in principle, a calibration factor from a reconstructed image needs to be determined for the exact same geometry and settings as the one where it is used. Calibration to raw projection data has the advantage of being independent of the reconstruction settings, or of the particular patient geometry. In the patient analysis, the dependence of the reconstructed counts on the reconstruction settings still needs to be considered but is preferably used as a part of separate corrections. In principle, this is a matter of separating the system sensitivity from geometry- and reconstruction-dependent effects, which we consider important for standardization.

When performing imaging of a patient to whom high activity has been administered, such as in therapy using ^{131}I, the camera can be saturated by the high rate of photon fluence, causing a loss of counts that results in underestimation of the activity [38]. Camera systems often act as combinations of: 1) paralyzable systems, where each event leads to dead time, regardless of whether the event is counted or not or 2) nonparalyzable systems, where subsequent events occurring during the dead time are ignored [35]. It should be noted that these system- characteristics models may be too simple to accurately describe modern digital systems that are able to buffer events into memory. In systems with this capability, the apparent dead-time can be reduced as compared to the actual system dead-time because the arrival times for the processing will be redefined and not equal to the true arrival times. This will allow for measurements of high count rates with less count loss and pile-up effects. The magnitude of the dead time effects is vendor-specific, where each has different types of proprietary solutions for compensation. Nevertheless, for quantitative imaging and dosimetry, it is important to investigate whether

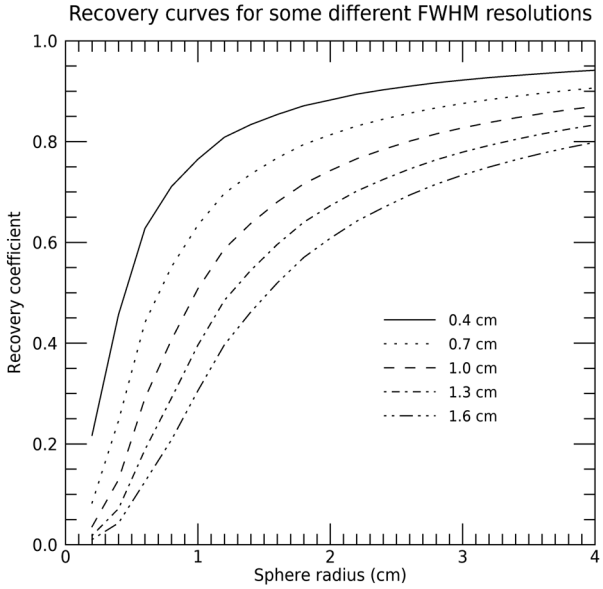

Fig. 4. Recovery coefficients for five different system spatial resolutions, modeled by a Gaussian point-spread function, for spheres of various radii.

dead time is of importance for the estimated quantities. For instance, in ^{177}Lu peptide receptor radionuclide therapy, where 7400 MBq is the standard activity administered, dead time effects may occur for images acquired soon after administration, even when the probability of photon emission is as low as 10.4%. However, since the magnitude of the TIAC is mainly governed by the images acquired at later times, the errors introduced by dead time are regarded as small in terms of absorbed dose estimates. Thus, in addition to the camera properties, the importance of dead time effects on absorbed dose estimates depends on the amount of administered activity, the radionuclide photon emission probability, and the pharmacokinetics of the compound used for therapy.

When the activity contained in a tissue volume is determined from the total count rate in a volume of interest (VOI) that is defined based on a high-resolution CT study, a loss of counts will occur due to resolution-induced spill-out, thus yielding an activity underestimate. Likewise, an increase of counts will occur due to spill-in from the surrounding activity. For small high-uptake volumes, the introduced error may be large (Fig. 4). These partial-volume effects are often corrected by employing recovery coefficients, defined as the ratios of the measured and true activity concentrations for different calibration objects [35]. The activity contained in the tissue volume $A(v)$ can then be determined using

$$A(v) = C_{\mathrm{VOI}} \cdot \frac{1}{S_{\mathrm{system}}} \cdot \frac{1}{RC(v)} \tag{5}$$

where C_{VOI} is the count rate in the VOI, S_{system} is the calibration factor (unit: $\mathrm{MBq}^{-1}\mathrm{s}^{-1}$), and $RC(v)$ is the recovery coefficient valid for the delineated tissue volume v. The recovery coefficients for different volumes and source shapes can be obtained by conducting physical phantom measurements or Monte Carlo simulations. Often spherical calibration objects are used, although the magnitude of the partial-volume effect

is dependent on the object shape, and the activity distribution both within the object and in the neighborhood of the object. The applicability of recovery coefficients thus needs to be validated for the geometry where they are used.

Automated methods for partial-volume compensation also exist and have been mainly applied in diagnostic SPECT and PET imaging, although they are relevant in the context of dosimetry, particularly for smaller structures such as tumors. Generally, such methods are model-based and attempt to determine the amount of resolution-induced spill-in and spill-out that result from limited spatial resolution. The corrections can be implemented in image space, i.e., on a voxel-basis or using predefined VOI templates for which the resolution-induced spill-in and spill-out are calculated [39].

IV. Absorbed Dose Calculations

Provided that accurate image quantification has been performed, the rate of energy absorption in each voxel can be calculated from the decay scheme of the radionuclide combined with a radiation energy transport model. When the voxel-wise mass distribution is available, which can be estimated from a CT image and mass-density calibration relationship, for instance, the energy distribution can easily be converted into an absorbed-dose-rate image. In relation to 1, the voxel-wise mean absorbed dose rate $\dot{D}_k(t)$ is given by

$$\dot{D}_k(t) = \frac{A_k(r_s, t)}{M_k(r_T, t)} \sum\nolimits_j \left[\Delta_j \cdot \phi_{vx}\left(r_T \leftarrow r_S, E_j, t\right)\right] \qquad (6)$$

where the subscript k designates the 3-D voxel coordinate.

The simplest procedure for calculating the absorbed-dose-rate distribution involves assuming that all of the emitted energy is absorbed in the voxel from which it was emitted, i.e., only considering the voxel self-dose. In (6), this technique requires setting the absorbed fractions for the emitted particles to unity. This assumption thus presupposes that the contribution to the dose absorbed by a given voxel from the other voxels is negligible. If the variation of the voxel mass density is disregarded and the mass density of, for instance, soft tissue, is assumed, the conversion from activity to absorbed dose rate is then a simple scaling procedure. However, this procedure is valid only if the range of the charged particles emitted upon radioactive decay is small compared with the voxel dimensions. Generally, the path length for photons is large compared to the typical voxel size, so the assumption of local energy absorption is often not valid for photons. Among the radionuclides used in therapy, ^{90}Y emits the β particles with the highest maximum energy (2.21 MeV). The continuous slowing down approximation (CSDA) range is very close to the average path length of an electron. It is calculated from the total stopping power of the electrons by assuming the energy loss at every point to be equal, disregarding any fluctuations in energy loss. The CSDA range is obtained by integrating the reciprocal of the total stopping power with respect to energy, which results in a maximum range of about 11.3 mm for ^{90}Y [40]. However, an electron interacts many times with random path direction changes. One alternative to using the CSDA range is employing the projected range, which is the average distance along the initial direction of the particle to which the particle will penetrate before coming to rest. A detour factor can be defined as the ratio of the projected range to the CSDA range, and this factor is always less than unity due to the multiple scattering. For electrons emitted by ^{90}Y, the detour factor in water is about 0.65 [41], which results in a projected range of 7.3 mm. Thus, in tissues with mass densities equal to or greater than that of water, it can be assumed that most of the kinetic energy is locally absorbed in the voxel from which it was emitted even for the highest β-particle energy used in radionuclide therapy, since the spatial resolution of a clinical SPECT image is generally larger than the radial distribution of energy.

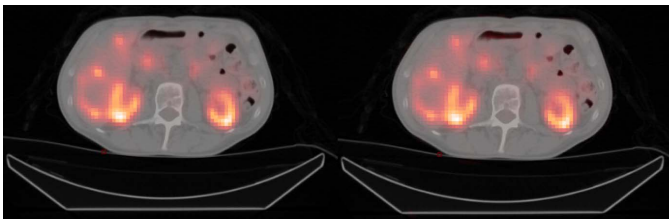

Fig. 5. Left: Quantitative SPECT/CT transversal slice over the kidney region. Right: Monte-Carlo-calculated absorbed-dose-rate image for the axial same position.

For photons that have mean free paths that are long compared to the spatial resolution, the radial distribution of energy from a point can be described using point-dose kernels. These functions can be obtained from Monte Carlo calculations. A quantitative SPECT image in units of activity can then be convolved with this point-source distribution to obtain an estimate of the deposited energy distribution. Point-dose kernels for mono-energetic electrons, photons, and complete decays have been published by many authors, starting with Berger in the late 1960s [42]–[44]. The functions are usually calculated in homogeneous media, making their usage less accurate in volumes with different tissue compositions or densities, but methods that scale with density have also been proposed [45], [46].

A full Monte Carlo calculation of the radiation transport provides the most accurate energy distribution calculation, in theory. The Monte Carlo program must be capable of reading 3-D image matrices and then performing radiation transport calculations from each voxel location in the SPECT image, using the assumption that the voxel value represents the activity in the voxel coordinate. The radiation transport is performed in a 3-D map of the interaction properties in tissue, which can be obtained from a co-registered CT study of the patient. The attenuation coefficients and stopping-power values required to calculate the various particle trajectories can be obtained by scaling the HU values of the CT image to the mass density [20], [33].

Fig. 5 shows a comparison of an SPECT image representing the activity distribution to a Monte-Carlo-calculated absorbed-dose-rate image. The images were acquired as part of a clinical trial (ILUMINET EUDRACT No 2011-000240-16) on the treatment of neuroendocrine tumors by ^{177}Lu-Dotatate. In this dosimetry-guided treatment protocol, the total number of treatment cycles is tailored according to the biological

effective dose (BED) received by the kidneys of each individual patient [47]. The acquired SPECT images are reconstructed using OS-EM, including corrections for attenuation, scatter using the ESSE method, and collimator resolution. Voxel-based Monte Carlo calculations are performed using the EGSnrc engine, with CT-derived mass-density images as input. As can be seen in Fig. 5, the images appear nearly identical and it is mainly the image values that change when going from activity to absorbed dose rate.

A. From Absorbed Dose Rate to Absorbed Dose

There are two equivalent means of obtaining the final estimate of the mean absorbed dose. One is to proceed according to 1 and first calculate the TIAC, i.e., the time integral of the activity $A(r_s, t)$, then apply model-based radiation-energy-transport values. The other is to calculate the absorbed dose rate for each imaging time point according to (6). The volumes in which the mean absorbed dose is calculated may be whole organs, parts of organs, or image voxels.

In both strategies, integration over time is required to estimate the area under the curve. Since data are usually sparsely sampled over time, the most common integration method involves interpolating between data points by fitting a curve to time-activity data and then performing analytical integration based on the curve-model function and fitted parameter values [48]. Such curve-fitting is usually performed based on the activity in the VOIs, but voxel-based curve-fitting and dosimetry methods have also been proposed [20], [49]–[51]. Curve shapes in the form of exponential functions are typically used, which generally well represent biological processes, such as uptake and washout of pharmaceuticals. Depending on the number of data points acquired, the curve shape can be modeled as the sum of exponential functions, whose rate constants and amplitudes must then be determined based on some optimization procedure, such as nonlinear least-squares fitting. If only one phase is included in the model, i.e., if the radiopharmaceutical washout is assumed to follow a mono-exponential function of time, then the amplitude and rate constant are often estimated by taking the logarithm of the data and applying linear regression, although linear regression theoretically requires the residuals to be distributed normally. As in any minimization, the initial parameter estimates must be performed with care and in a consistent manner for all patients. When possible, the uncertainty in the fitted model parameters can be propagated to estimate the combined uncertainty in the TIAC estimate and the absorbed dose.

An example application of voxel-based dosimetry is illustrated by a dosimetry-guided clinical trial of high-dose ^{90}Y-Zevalin^{TM} (Spectrum Pharmaceuticals) for the treatment of non-Hodgkin's lymphoma, which was performed at our center. The study protocol included both pretherapy and therapy imaging and was a dose-escalation study in terms of absorbed dose. Bone marrow stem cell support was included, and the administered activity was tailored to the next-in-line organ at risk, which was the liver. To determine the activity to administer to achieve the prescribed liver absorbed dose, ^{111}In-labeled Zevalin was administered pretherapy. ^{111}In-SPECT/CT studies were performed at seven points in time, and reconstructions with corrections for attenuation, scatter, and collimator resolution were conducted. The quantitative ^{111}In-SPECT images were then converted into ^{90}Y absorbed-dose-rate images by taking the differences in physical half-life into account and assuming local energy deposition of the (mimicked) ^{90}Y β particles. The images in the time series were co-registered using a nonrigid method, in which the CT images were used to determine the required spatial transformations that were also applied to the SPECT images [20]. The absorbed dose images were calculated on a voxel basis by trapezoidal integration and assuming physical decay from the last time point to infinity. The mean absorbed dose in the liver per unit of administered activity was then calculated and used to estimate the activity to administer for therapy. The absorbed doses delivered were also verified by ^{90}Y bremsstrahlung SPECT imaging at six points in time after the therapy administration and performing the same calculation steps as for ^{111}In-SPECT images. The patient study was not completed for clinical reasons, but the dosimetry protocol and results are described in more detail in [52] and [53].

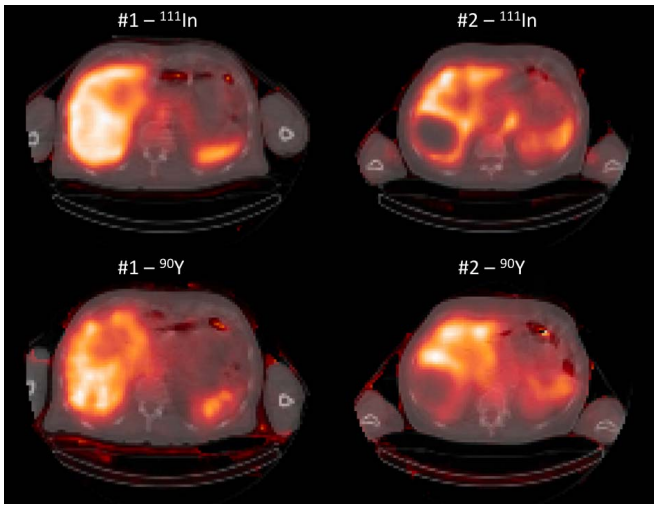

Fig. 6. Example of ^{90}Y absorbed dose maps of two patients acquired by performing pretherapy ^{111}In imaging (upper row) and peri-therapy ^{90}Y bremsstrahlung SPECT imaging (lower row).

Fig. 6 shows absorbed dose images for two patients as examples. Table III presents the results for the eight patients included, where it can be seen that the ^{111}In-predicted and delivered liver absorbed doses generally agree to within 2 Gy. For one patient (#3), the administered activity was completely entrapped in the liver and ^{90}Y therapy was prevented. With the standard protocol for ^{90}Y-Zevalin treatment, an activity of 14.8 MBq/kg is prescribed and imaging is generally not included.

In Table III, patients 1 and 2 had approximately the same weight (75 kg versus 79 kg), meaning that the liver absorbed doses delivered to these patients would have differed by a factor of 1.7 if the standard protocol were applied. For patient #3, the therapy would not have been useful and would have produced unnecessary patient exposure and health care costs.

TABLE III
ABSORBED DOSE COEFFICIENTS FOR LIVER DETERMINED FROM ^{111}IN PRETHERAPY STUDIES, TARGETED ABSORBED DOSE, ACTUALLY ADMINISTERED ^{90}Y ACTIVITY, AND LIVER ABSORBED DOSE OBTAINED FROM INTRATHERAPY ^{90}Y BREMSSTRAHLUNG IMAGING

	From ^{111}In imaging		^{90}Y Therapy	
Patient #	^{90}Y Dose/Aadm (Gy/GBq)	Target Dose (Gy)	Aadm (MBq)	Abs Dose (Gy)
1	4.1	12	2915	10.3
2	2.4	12	4990	13.0
3	20.2	12	N/A	N/A
4	6.4	12	1825	10.2
5	3.9	17.2	4445	15.1
6	4.4	17.2	3905	16.6
7	4.6	17.2	3780	16.0
8	3.4	21.5	6080	19.4

B. Modifying Factors and the Connection Between Absorbed Dose and Radiobiological Response

Experiences with other forms of radiotherapy have demonstrated the existence of several time-dependent factors that modify the radiobiological response, including fractionation, the absorbed dose rate (depending on the tissue repair capacity), the concentration of oxygen in the irradiated tissue, and cell proliferation and cell-cycle progression during irradiation [54]. In radionuclide therapy, the mean absorbed dose rate is lower than in most other forms of radiotherapy, it varies over time, often in an exponentially decreasing manner, and the uptake can be imaged over long times (on the order of days or even weeks) [55]. As example values from our experience in ^{177}Lu-Dotatate therapy, the absorbed dose rate for kidneys at around 24 h after administration of 7400 MBq is approximately 40–100 mGy/h, with an effective half-time of 40–60 h. The corresponding values for metastases are approximately 20–300 mGy/h, with an effective half-time of 60–150 h (preliminary data). This can be compared to the typical 1 Gy/min in external beam radiotherapy, which is, thus, approximately three orders of magnitude higher. Although the main evidence of the effects of modifying radiobiological factors is from other forms of radiotherapy, clinical evidence in radionuclide therapy is emerging. For instance, Barone *et al.* [56] found that kidney toxicity in patients with neuroendocrine tumors treated using ^{90}Y-Dotatoc treatment could be better explained by accounting for the effects of absorbed dose rate and fractionation. The oxygen effect was investigated by Walrand *et al.* [57], who found that the correlation between the absorbed dose and the responses of hepatic lesions in patients treated with ^{90}Y-labeled microspheres was improved by considering hemoglobin status. In addition to the above-mentioned factors, in radionuclide therapy there is spatial inhomogeneity in the absorbed dose delivery governed by the internal distribution of the radionuclide combined with the range of the particles emitted upon radioactive decay. The effects of the small-scale inhomogeneity in the absorbed dose delivery is difficult to address in clinical situations, and the approaches taken mainly involve models based on preclinical or reference data. A notable contribution in this context is the work by Konijnenberg *et al.* [58] who investigated the small-scale distribution of ^{111}In-DTPA-octreotide in human kidneys.

In the linear-quadratic radiobiological model, the BED concept has been widely used in external-beam and brachytherapy to account for the effects of fractionation and the absorbed dose rate. A more general quantity, the equi-effective dose (EQDX) was established in 2012 by the International Commission on Radiation Units and Measurements (ICRU), for which BED is a special case [59]. The effect of the absorbed dose rate was not explicitly included in the EQDX formulation but can easily be obtained by combination with the previously presented equations. Generally, for protracted irradiation, the effects of repair during exposure are accounted for by the so-called Lea-Catcheside factor $G(T)$, which is defined by

$$G(T) = \frac{2}{D^2}\int_0^{T_D} R(t)\left[\int_0^t R(w)\varphi(t-w)\mathrm{d}w\right]\mathrm{d}t \tag{7}$$

where T_D is the total irradiation time, $R(t)$ is the absorbed dose rate as a function of time, and $\varphi(t)$ is a function describing the loss of sublethal lesions due to repair [60]–[62]. If irradiation is performed in a *test* situation, for instance, in one single fraction with total absorbed dose D and absorbed dose rate $R(t)$, and a specific biological effect is obtained, then the EQDX is the total absorbed dose required to induce the same biological effect when irradiation is performed under reference conditions, where X denotes the dose fraction. EQD2 is often used, implying that the reference conditions include 2 Gy fractions delivered at a high dose rate. The BED is equivalent to EQD0, i.e., when the reference situation is such that the absorbed dose is given in an infinite number of infinitesimally small fractions, or at a very low dose rate. The BED (or EQD0) for the test situation described above can then be written as

$$\mathrm{BED} = \mathrm{EQD0}_{\alpha/\beta} = D\left(1 + \frac{G(T)\cdot D}{\alpha/\beta}\right) \tag{8}$$

where α/β is an endpoint-specific radiobiological model parameter.

V. DOSIMETRY AND PET

The importance of PET in radionuclide therapy lies mainly in the diagnostic step for patient selection, treatment planning, and response monitoring mainly because of the superior quality of PET images as compared to SPECT images and the fact that there are only a few long-lived positron-emitting radionuclides that can produce therapeutic absorbed doses to target volumes [63].

^{124}I is a PET radionuclide with a 4.2-day half-life that is applicable in dosimetry for ^{131}I treatment of differentiated thyroid cancer [51], [64]. Because of its long half-life, it can be used to determine the biokinetics of radioiodine with an improved image quality as compared to ^{131}I SPECT [65]. Positrons with maximum kinetic energies of 1535 keV and

2138 keV are emitted in 23% of the transitions. ^{124}I also emits several gamma-photons upon decay, and the 603 keV and 723 keV photons especially (with 63% and 10% abundances, respectively) can generate random coincidences with the 511 keV annihilation photons, thus affecting the PET image quality.

Previously, ^{111}In-labeled Octeotide combined with SPECT or planar imaging was widely used for patients with neuroendocrine tumors. The images suffered from poor spatial resolution, and nowadays many clinical centers have adopted ^{68}Ga-Dotatate/Dotatoc PET/CT to achieve improved image quality [66].

^{89}Zirconium is a potential radionuclide for patient selection and therapy monitoring [67]. ^{89}Zr decays via positron emission and electron capture through meta-stable ^{89}Y^{m} to stable ^{89}Y. The kinetic energy of the positrons is 395 keV on average. Due to the long half-life of 78.4 h, PET imaging with ^{89}Zr has been proposed as a dosimetry tool for subsequent ^{90}Y therapy [68].

One application that has become common is ^{90}Y PET imaging. The decay of ^{90}Y to ^{90}Zr has a minor branch to the 0^{+} first excited state of ^{90}Zr at 1.76 MeV, which is followed by β^{+}/β^{-} emission. However, the ^{90}Y positron branching factor, where two 511 keV annihilation photons are produced, is only 0.0032% [69], implying problems with noise in the imaging. The main clinical application of ^{90}Y PET has been in radioembolization treatment of primary liver cancer or metastases in the liver, where ^{90}Y-labeled microspheres of glass or resin are administered intra-arterially. Because the concentration of ^{90}Y-labeled micro-spheres in the liver is comparably high, sufficient coincidence rates can be obtained even with the small positron branching factor. However, the false coincidences that occur when single annihilation photons are detected together with the bremsstrahlung emitted from the patient cause problems in ^{90}Y PET imaging. This bremsstrahlung is generated when the β^{-} particles emitted upon the decay of ^{90}Y interact in the patient. The bremsstrahlung photons has a continuous energy distribution ranging up to 2.3 MeV with an abundance per decay of $\approx$2% above 50 keV and $\approx$0.14% in the acquisition energy window [70]. In addition, the LYSO scintillator crystals used in many PET scanners contain traces of radioactive ^{176}Lu, which emits photons with three main energies 88, 203, and 307 keV. The interactions from these photons will also contribute to random coincidences [71], [72].

^{86}Y has a half-life of 14.74 h. It decays by positron emission (33%) or electron capture (66%) to ^{86}Sr, followed by the emission of a cascade of high-energy γ-rays. In dosimetry, ^{86}Y is mainly employed in the pretherapy step to determine the biodistribution of ^{90}Y-labeled radiopharmaceuticals used for therapy [73]. ^{86}Y-Dotatoc has been successfully utilized for dosimetry in ^{90}Y peptide receptor radionuclide therapy [10], [56].

VI. Discussion

A. Factors to Consider in Image-Based Dosimetry

Voxel-based dosimetry is based on activity or activity concentration quantification for each voxel coordinate, from which the deposited radiation energy distribution is calculated. By dividing the absorbed energy by the voxel mass, the absorbed dose is calculated. Technically, when the image has been segmented, a frequency histogram of the activity or absorbed dose values in a volume can be derived. The image information can then be analyzed by employing differential or integral dose-volume histograms (DVHs). However, it must be kept in mind that even when the voxel activity or voxel absorbed dose has been obtained from accurate quantitative SPECT or PET images, possibly combined with accurate radiation transport code, variations in the absorbed dose distribution are also caused by limitations in the imaging process. In particular, the blurring effects introduced by the spatial resolution of the underlying tomographic system affect the apparent activity concentration in a particular voxel and, consequently, the calculated dose absorbed at that voxel location.

Improved image resolution can be obtained by including collimator compensation in the tomographic reconstruction, which is now possible with most commercial PET and SPECT systems. However, there is an increasing awareness of the edge artefacts that appear with these compensations, in the form of ring-shaped patterns [26], [39] that appear close to sharp boundaries, in particular. A decrease in counts in the central region of a symmetrical object can also be generated, which can be falsely interpreted as decreased uptake. Although this effect does not alter the total number of counts in the image, it creates image patterns that do not accurately reflect the activity distribution in the patient. Thus, the representativeness of DVHs in radionuclide therapy dosimetry needs to be carefully investigated before interpretation.

To work efficiently with quantitative SPECT and related dosimetry calculation, the community should encourage vendors to use floating-point numbers instead of integer values. Although the floating-point data type is not generally supported by the DICOM standard, this data type would better accommodate the calculation of image values in units of Bq or Gy if it could be used. Additional advantages are that number truncation, the potential risk of overflow in voxel values, and scaling problems could be avoided. Another important future development would be to include in the DICOM standard public tags for dosimetry-related information, such as calibration factors, iteration and subset parameters, and other information related to absorbed dose calculations.

Yet another desired possibility is to allow clinical work station users to upload user-specific filter kernels. Tools for low-pass filtering for noise reduction have already been implemented at most nuclear medicine workstations. Convolution with a point-dose kernel is a similar and straightforward procedure and implementation at clinical work stations would not be difficult if vendors would allow user-specific input of such functions.

B. Is Dosimetry Worth the Effort?

Among the clinically used radiotherapy modalities, dosimetry-guided treatment in radionuclide therapy has been the slowest to develop. A technical obstacle has been the unavailability of quantitative SPECT imaging in clinical

systems, since this method has been limited to the more research-oriented centers. With the introduction of hybrid SPECT/CT systems in the early 2000s with hardware-based co-registration of anatomical and functional images, many of the earlier obstacles were eliminated. Iterative ML-EM/OS-EM reconstruction methods combined with CT-based attenuation, collimator resolution compensation, and scatter correction are now more or less standard methods, which could also be optimized for the radionuclides used in radionuclide therapy with help from vendors. Several vendors currently offer quantitative SPECT, as well as dosimetry packages, in their clinical software.

There are also logistical challenges involved in dosimetry, since images need to be acquired on several occasions, and, thus, more steps are involved than in a single nuclear medicine examination. It may be more or less straightforward to incorporate dosimetric studies into the logistics of nuclear medicine departments, for instance, when therapy patients need to be measured at certain times. Moreover, image series evaluation is easier if the patient has similar positions in each series; thus, it is preferable for the patient to be positioned on the couch in a reproducible way, preferably assisted by directional lasers. Other challenges in the implementation of dosimetry-guided treatment involve the post-acquisition computational steps, i.e., the availability of methods and software, in which the drawing of VOIs can involve a substantial workload.

As in any kind of radiotherapy, dosimetry requires teamwork and presupposes the combined competence of physicians, medical physicists, and technologists. In an ongoing clinical trial at our center for the treatment of neuroendocrine tumors using ^{177}Lu-Dotatate, dosimetry is performed in every treatment cycle, by using four imaging time points in each case, which introduces a non-negligible workload. For its implementation, a workflow inspired by external beam radiotherapy routines was developed, where, in addition to the physicists, the technologists have a key role and are engaged in the drawing of VOIs as well as dosimetric calculations. The physicists are responsible for method development, calibration measurements, supervision, and double-checking of all of the values to be reported to the oncologist. Without this organization and teamwork, it would not have been possible to realize the dosimetry-guided therapy approach in the trial.

In addition to the technical challenges involved, there is an ongoing discussion of the benefits of implementing individual-based dosimetry in clinical radionuclide therapy, as an alternative to prescriptions based on a fixed-activity posology. Chiesa *et al.* [74] drew attention to the current inconsistency between the posology described on the inserts inside many therapeutic radiopharmaceutical packages and the European Directive [11]. In principle, the directive should prevent the administration of radioactive compounds for therapeutic purposes without consideration of the absorbed doses delivered to the individual patient. The editorial by Chiesa *et al.* [74] also detailed different strategies for dosimetry implementation in radionuclide therapy, with respect to either the doses absorbed by target tissues or the risk of inducing toxicity in normal organs, using the so-called "as high as safely attainable" approach. Giamarille *et al.* [75], [76] represented a quite different view and questioned many of the statements made by Chiesa *et al.* In their opinion, radionuclide therapy is "better characterized as a tumor-selective treatment modality with more similarities to systemic chemotherapy." Flux *et al.* [77] responded to the letter by Giamarille *et al.* and argued for the introduction of dosimetry, starting from the basic knowledge that the absorbed dose is the quantity that is primarily used to estimate the probability of inducing radiobiological effects in tissue, in any human use of radiation. Eberlein *et al.* [78] followed the same line of argument, with focus on the possibilities offered by theranostic approaches, and emphasized the additional value of individual-based dosimetry in this context.

In a recent survey across European countries, the current practice of dosimetry-guided radionuclide therapy in clinical practice and research studies was investigated. Not unexpectedly, it was found that the most common type of radionuclide therapy is still ^{131}I-NaI treatment of benign thyroid diseases. One of the countries in which this therapy was reported to include dosimetry always or most of the time was Sweden. The current national legislations in Sweden state that nuclear medicine treatment should be undertaken under the responsibility of a physician with specialist competence in oncology [79]. We believe that there may be a connection between the specialty of the responsible physician and interest and willingness to prioritize personalized treatments, including dosimetry for therapy guidance.

VII. Conclusion

Treatment individualization is currently of interest in many different kinds of cancer treatment, both medical and radiotherapeutic. Radionuclide therapy has the advantages that the agent responsible for the therapeutic effect can be monitored over time and that its concentration can be quantified. These characteristics pave the way for patient-specific dosimetry and therapy guidance based on dosimetry. Should we close our eyes to these opportunities?

References

[1] K. S. Gleisner *et al.*, "Variations in the practice of molecular radiotherapy and implementation of dosimetry: Results from a European survey," *EJNMMI Phys.*, vol. 4, no. 1, p. 28, Dec. 2017.

[2] C. Stokke *et al.*, "Dosimetry-based treatment planning for molecular radiotherapy: A summary of the 2017 report from the internal dosimetry task force," *EJNMMI Phys.*, vol. 4, no. 1, p. 27, Nov. 2017.

[3] L. Strigari *et al.*, "The evidence base for the use of internal dosimetry in the clinical practice of molecular radiotherapy," *Eur. J. Nucl. Med. Mol. Imag.*, vol. 41, no. 10, pp. 1976–1988, Oct. 2014.

[4] C. Chiesa *et al.*, "Radioembolization of hepatocarcinoma with (90)Y glass microspheres: Development of an individualized treatment planning strategy based on dosimetry and radiobiology," *Eur. J. Nucl. Med. Mol. Imag.*, vol. 42, no. 11, pp. 1718–1738, Oct. 2015.

[5] O. Chansanti *et al.*, "Tumor dose response in yttrium-90 resin microsphere embolization for neuroendocrine liver metastases: A tumor-specific analysis with dose estimation using SPECT-CT," *J. Vascu. Intervent. Radiol.*, vol. 28, no. 11, pp. 1528–1535, Nov. 2017.

[6] A. F. van den Hoven *et al.*, "Insights into the dose-response relationship of radioembolization with resin 90Y-microspheres: A prospective cohort study in patients with colorectal cancer liver metastases," *J. Nucl. Med.*, vol. 57, no. 7, pp. 1014–1019, Jul. 2016.

[7] L. Strigari *et al.*, "Efficacy and toxicity related to treatment of hepatocellular carcinoma with 90Y-SIR spheres: Radiobiologic considerations," *J. Nucl. Med.*, vol. 51, no. 9, pp. 1377–1385, Sep. 2010.

[8] M. Cremonesi *et al.*, "Correlation of dose with toxicity and tumour response to ^{90}Y-and ^{177}Lu-PRRT provides the basis for optimization through individualized treatment planning," *Eur. J. Nucl. Med. Mol. Imag.*, pp. 1–16, May 2018, doi: 10.1007/s00259-018-4044-x.

[9] E. Ilan *et al.*, "Dose response of pancreatic neuroendocrine tumors treated with peptide receptor radionuclide therapy using 177Lu-DOTATATE," *J. Nucl. Med.*, vol. 56, no. 2, pp. 177–182, Feb. 2015.

[10] S. Pauwels *et al.*, "Practical dosimetry of peptide receptor radionuclide therapy with (90)Y-labeled somatostatin analogs," *J. Nucl. Med.*, vol. 46, no. S1, pp. 92S–98S, Jan. 2005.

[11] "Council directive 2013/59/Euratom," vol. 57, 2014. [Online]. Available: https://eur-lex.europa.eu/legal-content/EN/TXT/HTML/?uri=CELEX:32013L0059&from=EN

[12] W. E. Bolch, K. F. Eckerman, G. Sgouros, and S. R. Thomas, "MIRD pamphlet no. 21: A generalized schema for radiopharmaceutical dosimetry–standardization of nomenclature," *J. Nucl. Med.*, vol. 50, no. 3, pp. 477–484, Mar. 2009.

[13] "ICRP publication 110. Adult reference computational phantoms," *Ann. ICRP*, vol. 39, no. 2, pp. 1–166, 2009. [Online]. Available: http://www.icrp.org/publication.asp?id=icrp%20publication%20110

[14] W. E. Bolch *et al.*, "ICRP Publication 133. The ICRP computational framework for internal dose assessment for reference adults: Specific absorbed fractions," *Ann. ICRP*, vol. 45, no. 2, p. 74, 2016.

[15] G. Sgouros, R. F. Hobbs, and H. Song, "Modelling and dosimetry for alpha-particle therapy," *Current Radiopharmaceuticals*, vol. 4, no. 3, pp. 261–265, Jul. 2011.

[16] J. Gustafsson, A. Sundlov, and K. S. Gleisner, "SPECT image segmentation for estimation of tumour volume and activity concentration in ^{177}Lu-DOTATATE radionuclide therapy," *EJNMMI Res.*, vol. 7, no. 1, p. 18, Dec. 2017.

[17] H. M. Hudson and R. S. Larkin, "Accelerated image reconstruction using ordered subsets of projection data," *IEEE Trans. Med. Imag.*, vol. 13, no. 4, pp. 601–609, Dec. 1994.

[18] P. E. Kinahan, D. W. Townsend, T. Beyer, and D. Sashin, "Attenuation correction for a combined 3D PET/CT scanner," *Med. Phys.*, vol. 25, no. 10, pp. 2046–2053, Oct. 1998.

[19] K. H. Wong, H. R. Tang, G. Segall, and B. H. Hasegawa, "Development of quantitative imaging methods for the GE Hawkeye CT/SPECT system," presented at the IEEE Nucl. Sci. Symp. Conf. Rec., San Diego, CA, USA, Nov. 2002.

[20] K. Sjogreen-Gleisner, D. Rueckert, and M. Ljungberg, "Registration of serial SPECT/CT images for three-dimensional dosimetry in radionuclide therapy," *Phys. Med. Biol.*, vol. 54, no. 20, pp. 6181–6200, Oct. 2009.

[21] K. Ogawa, Y. Harata, T. Ichihara, A. Kubo, and S. Hashimoto, "A practical method for position-dependent Compton-scatter correction in single photon emission CT," *IEEE Trans. Med. Imag.*, vol. 10, no. 3, pp. 408–412, Sep. 1991.

[22] B. Axelsson, P. Msaki, and A. Israelsson, "Subtraction of Compton-scattered photons in single-photon emission computerized tomography," *J. Nucl. Med.*, vol. 25, no. 4, pp. 490–494, 1984.

[23] M. Ljungberg and S. E. Strand, "Scatter and attenuation correction in SPECT using density maps and Monte-Carlo simulated scatter functions," *J. Nucl. Med.*, vol. 31, no. 9, pp. 1560–1567, Sep. 1990.

[24] E. C. Frey and B. M. W. Tsui, "A new method for modeling the spatially-variant, object-dependent scatter response function in SPECT," in *Proc. Conf. Rec. IEEE Med. Imag.*, Anaheim, CA, USA, Nov. 1996, pp. 1082–1086.

[25] H. Zaidi and M.-L. Montandon, "Scatter compensation techniques in PET," *PET Clinics*, vol. 2, no. 2, pp. 219–234, Apr. 2007.

[26] A. Rahmim, J. Qi, and V. Sossi, "Resolution modeling in PET imaging: Theory, practice, benefits, and pitfalls," *Med. Phys.*, vol. 40, no. 6, Jun. 2013, Art. no. 064301.

[27] N. Anizan *et al.*, "Factors affecting the stability and repeatability of gamma camera calibration for quantitative imaging applications based on a retrospective review of clinical data," *EJNMMI Res.*, vol. 4, no. 1, p. 67, Dec. 2014.

[28] N. Anizan, H. Wang, X. C. Zhou, R. L. Wahl, and E. C. Frey, "Factors affecting the repeatability of gamma camera calibration for quantitative imaging applications using a sealed source," *Phys. Med. Biol.*, vol. 60, no. 3, pp. 1325–1337, Feb. 2015.

[29] W. Zhao *et al.*, "Determination of gamma camera calibration factors for quantitation of therapeutic radioisotopes," *EJNMMI Phys.*, vol. 5, no. 1, p. 8, May 2018.

[30] A. Halty, J.-N. Badel, O. Kochebina, and D. Sarrut, "Image-based SPECT calibration based on the evaluation of the fraction of activity in the field of view," *EJNMMI Phys.*, vol. 5, no. 1, p. 11, May 2018.

[31] M. D'Arienzo *et al.*, "Gamma camera calibration and validation for quantitative SPECT imaging with (177)Lu," *Appl. Radiat. Isotopes*, vol. 112, pp. 156–164, Jun. 2016.

[32] J. Gustafsson *et al.*, "Uncertainty propagation for SPECT/CT-based renal dosimetry in (177)Lu peptide receptor radionuclide therapy," *Phys. Med. Biol.*, vol. 60, no. 21, pp. 8329–8346, Nov. 2015.

[33] K. Sjögreen, M. Ljungberg, and S. E. Strand, "An activity quantification method based on registration of CT and whole-body scintillation camera images, with application to 131I," *J. Nucl. Med.*, vol. 43, no. 7, pp. 972–982, Jul. 2002.

[34] M. D'Arienzo and M. Cox, "Uncertainty analysis in the calibration of an emission tomography system for quantitative imaging," *Comput. Math. Methods Med.*, vol. 2017, 2017, Art. no. 9830386. [Online]. Available: https://www.hindawi.com/journals/cmmm/2017/9830386/

[35] Y. K. Dewaraja *et al.*, "MIRD pamphlet no. 23: Quantitative SPECT for patient-specific 3-dimensional dosimetry in internal radionuclide therapy," *J. Nucl. Med.*, vol. 53, no. 8, pp. 1310–1325, Aug. 2012.

[36] J. C. Sanders, T. Kuwert, J. Hornegger, and P. Ritt, "Quantitative SPECT/CT imaging of (177)Lu with in vivo validation in patients undergoing peptide receptor radionuclide therapy," *Mol. Imag. Biol.*, vol. 17, no. 4, pp. 585–593, Aug. 2015.

[37] F. Bouchet *et al.*, "Calibration test of PET scanners in a multi-centre clinical trial on breast cancer therapy monitoring using 18F-FLT," *PLoS ONE*, vol. 8, no. 3, 2013, Art. no. e58152.

[38] Y. K. Dewaraja *et al.*, "MIRD pamphlet no. 24: Guidelines for quantitative 131I SPECT in dosimetry applications," *J. Nucl. Med.*, vol. 54, no. 12, pp. 2182–2188, Dec. 2013.

[39] K. Erlandsson, I. Buvat, P. H. Pretorius, B. A. Thomas, and B. F. Hutton, "A review of partial volume correction techniques for emission tomography and their applications in neurology, cardiology and oncology," *Phys. Med. Biol.*, vol. 57, no. 21, pp. 119–159, Nov. 2012.

[40] "Stopping powers for electrons and positrons," Int. Commission Radiat. Units Meas., Bethesda, MD, USA, Rep. 37, 1984.

[41] J. M. Fernandez-Varea, P. Andreo, and T. Tabata, "Detour factors in water and plastic phantoms and their use for range and depth scaling in electron-beam dosimetry," *Phys. Med. Biol.*, vol. 41, no. 7, pp. 1119–1139, Jul. 1996.

[42] M. J. Berger, "Energy deposition in water by photons from point isotropic sources: MIRD pamphlet no. 2," *J. Nucl. Med.*, vol. 9, no. 1, pp. 15–25, 1968.

[43] M. J. Berger, "Distribution of absorbed dose around point sources of electrons and beta particles in water and other media: MIRD pamphlet no. 7," *J. Nucl. Med.*, vol. 12, pp. 5–23, Mar. 1971.

[44] M. Pacilio *et al.*, "Differences in 3D dose distributions due to calculation method of voxel S-values and the influence of image blurring in SPECT," *Phys. Med. Biol.*, vol. 60, no. 5, pp. 1945–1964, Mar. 2015.

[45] A. Dieudonné *et al.*, "Study of the impact of tissue density heterogeneities on 3-dimensional abdominal dosimetry: Comparison between dose kernel convolution and direct Monte Carlo methods," *J. Nucl. Med.*, vol. 54, no. 2, pp. 236–243, Feb. 2013.

[46] M. Sanchez-Garcia, I. Gardin, R. Lebtahi, and A. Dieudonné, "Implementation and validation of collapsed cone superposition for radiopharmaceutical dosimetry of photon emitters," *Phys. Med. Biol.*, vol. 60, no. 20, pp. 7861–7876, Oct. 2015.

[47] A. Sundlöv *et al.*, "Individualised ^{177}Lu-DOTATATE treatment of neuroendocrine tumours based on kidney dosimetry," *Eur. J. Nucl. Med. Mol. Imag.*, vol. 44, no. 9, pp. 1480–1489, Mar. 2017.

[48] P. Kletting and G. Glatting, "Model selection for time-activity curves: The corrected Akaike information criterion and the F-test," *Z Med. Phys.*, vol. 19, no. 3, pp. 200–206, 2009.

[49] D. Sarrut, A. Halty, J. N. Badel, L. Ferrer, and M. Bardiès, "Voxel-based multimodel fitting method for modeling time activity curves in SPECT images," *Med. Phys.*, vol. 44, no. 12, pp. 6280–6288, Dec. 2017.

[50] P. A. Jackson *et al.*, "An automated voxelized dosimetry tool for radionuclide therapy based on serial quantitative SPECT/CT imaging," *Med. Phys.*, vol. 40, no. 11, Nov. 2013, Art. no. 112503.

[51] G. Sgouros *et al.*, "Patient-specific dosimetry for 131I thyroid cancer therapy using 124I PET and 3-dimensional-internal dosimetry (3D-ID) software," *J. Nucl. Med.*, vol. 45, no. 8, pp. 1366–1372, 2004.

[52] D. Minarik *et al.*, "90Y Bremsstrahlung imaging for absorbed-dose assessment in high-dose radioimmunotherapy," *J. Nucl. Med.*, vol. 51, no. 12, pp. 1974–1978, 2010.

[53] K. Sjogreen-Gleisner *et al.*, "Dosimetry in patients with B-cell lymphoma treated with [90Y]ibritumomab tiuxetan or [131I]tositumomab," *Quart. J. Nucl. Med. Mol. Imag.*, vol. 55, no. 2, pp. 126–154, 2011.

[54] E. J. Hall and A. J. Giaccia, *Radiobiology for the Radiologist*, 6th ed. Philadelphia, PA, USA: Lippincott Williams & Wilkins, 2006, pp. 1–546.

[55] K. S. Gleisner *et al.*, "Long-term retention of 177Lu/177mLu-DOTATATE in patients investigated by gamma-spectrometry and gamma-camera imaging," *J. Nucl. Med.*, vol. 56, no. 7, pp. 976–984, Jul. 2015.

[56] R. Barone *et al.*, "Patient-specific dosimetry in predicting renal toxicity with (90)Y-DOTATOC: Relevance of kidney volume and dose rate in finding a dose-effect relationship," *J. Nucl. Med.*, vol. 46, pp. 99S–106S, Jan. 2005.

[57] S. Walrand *et al.*, "Hemoglobin level significantly impacts the tumor cell survival fraction in humans after internal radiotherapy," *EJNMMI Res.*, vol. 2, no. 1, p. 20, May 2012.

[58] M. Konijnenberg, M. Melis, R. Valkema, E. Krenning, and M. de Jong, "Radiation dose distribution in human kidneys by octreotides in peptide receptor radionuclide therapy," *J. Nucl. Med.*, vol. 48, no. 1, pp. 134–142, Jan. 2007.

[59] S. M. Bentzen *et al.*, "Bioeffect modeling and equieffective dose concepts in radiation oncology—Terminology, quantities and units," *Radiotherapy Oncol.*, vol. 105, no. 2, pp. 266–268, Nov. 2012.

[60] J. Gustafsson, P. Nilsson, and K. S. Gleisner, "On the biologically effective dose (BED)-using convolution for calculating the effects of repair: II. Numerical considerations," *Phys. Med. Biol.*, vol. 58, no. 5, pp. 1529–1548, Mar. 2013.

[61] J. Gustafsson, P. Nilsson, and K. S. Gleisner, "On the biologically effective dose (BED)-using convolution for calculating the effects of repair: I. Analytical considerations," *Phys. Med. Biol.*, vol. 58, no. 5, pp. 1507–1527, Mar. 2013.

[62] A. M. Kellerer and H. H. Rossi, "The theory of dual radiation action," in *Current Topics in Radiation Research*, vol. 8, M. Ebert and A. Howard, Eds. Amsterdam, The Netherlands: North Holland, 1974, pp. 85–158.

[63] M. Blaickner and R. P. Baum, "Relevance of PET for pretherapeutic prediction of doses in peptide receptor radionuclide therapy," *PET Clinics*, vol. 9, no. 1, pp. 99–112, Jan. 2014.

[64] W. Jentzen *et al.*, "Optimized 124I PET dosimetry protocol for radioiodine therapy of differentiated thyroid cancer," *J. Nucl. Med.*, vol. 49, no. 6, pp. 1017–1023, Jun. 2008.

[65] R. Kuker, M. Sztejnberg, and S. Gulec, "I-124 imaging and dosimetry," *Mol. Imag. Radionuclide Ther.*, vol. 26, no. 1, pp. 66–73, Feb. 2017.

[66] A. Mojtahedi, S. Thamake, I. Tworowska, D. Ranganathan, and E. S. Delpassand, "The value of (68)Ga-DOTATATE PET/CT in diagnosis and management of neuroendocrine tumors compared to current FDA approved imaging modalities: A review of literature," *Amer. J. Nucl. Med. Mol. Imag.*, vol. 4, no. 5, pp. 426–434, 2014.

[67] F. C. J. van de Watering *et al.*, "Zirconium-89 labeled antibodies: A new tool for molecular imaging in cancer patients," *BioMed. Res. Int.*, vol. 2014, p. 13, May 2014. [Online]. Available: https://www.ncbi.nlm.nih.gov/pubmed/24991539

[68] S. N. Rizvi *et al.*, "Biodistribution, radiation dosimetry and scouting of 90Y-ibritumomab tiuxetan therapy in patients with relapsed B-cell non-Hodgkin's Lymphoma using 89Zr-ibritumomab tiuxetan and PET," *Eur. J. Nucl. Med. Mol. Imag.*, vol. 39, no. 3, pp. 512–520, Mar. 2012.

[69] R. G. Selwyn, R. J. Nickles, B. R. Thomadsen, L. A. DeWerd, and J. A. Micka, "A new internal pair production branching ratio of 90Y: The development of a non-destructive assay for 90Y and 90Sr," *Appl. Radiat. Isot.*, vol. 65, no. 3, pp. 318–327, Mar. 2007.

[70] X. Rong *et al.*, "Development and evaluation of an improved quantitative (90)Y bremsstrahlung SPECT method," *Med. Phys.*, vol. 39, no. 5, pp. 2346–2358, May 2012.

[71] J. Strydhorst, T. Carlier, A. Dieudonne, M. Conti, and I. Buvat, "A gate evaluation of the sources of error in quantitative ^{90}Y PET," *Med. Phys.*, vol. 43, no. 10, pp. 5320–5329, Oct. 2016.

[72] M. Conti *et al.*, "Characterization of (176)Lu background in LSO-based PET scanners," *Phys. Med. Biol.*, vol. 62, no. 9, pp. 3700–3711, May 2017.

[73] J. Huang, L. Cui, F. Wang, and Z. Liu, "PET tracers based on (86)Y," *Current Radiopharmaceuticals*, vol. 4, no. 2, pp. 122–130, Apr. 2011.

[74] C. Chiesa *et al.*, "The conflict between treatment optimization and registration of radiopharmaceuticals with fixed activity posology in oncological nuclear medicine therapy," *Eur. J. Nucl. Med. Mol. Imag.*, vol. 44, no. 11, pp. 1783–1786, 2017.

[75] F. Giammarile *et al.*, "Dosimetry in clinical radionuclide therapy: The devil is in the detail," *Eur. J. Nucl. Med. Mol. Imag.*, vol. 44, no. 12, pp. 1–3, Nov. 2017.

[76] F. Giammarile *et al.*, "Correction to: Dosimetry in clinical radionuclide therapy: The devil is in the detail," *Eur. J. Nucl. Med. Mol. Imag.*, vol. 45, no. 4, p. 679, Jan. 2018.

[77] G. D. Flux *et al.*, "From fixed activities to personalized treatments in radionuclide therapy: Lost in translation?" *Eur. J. Nucl. Med. Mol. Imag.*, vol. 45, no. 1, pp. 152–154, Jan. 2018.

[78] U. Eberlein, M. Cremonesi, and M. Lassmann, "Individualized dosimetry for theranostics: Necessary, nice to have, or counterproductive?" *J. Nucl. Med.*, vol. 58, pp. 97S–103S, Sep. 2017.

[79] R. Boellaard *et al.*, "FDG PET and PET/CT: EANM procedure guidelines for tumour PET imaging: Version 1.0," *Eur. J. Nucl. Med. Mol. Imag.*, vol. 37, no. 1, pp. 181–200, Jan. 2010.